

Particle acceleration in three-dimensional tearing configurationsChristoph Nodes[†], Guido T. Birk, Harald Lesch, and Rüdiger Schopper

Institute for Astronomy and Astrophysics

University of Munich, Germany

also: Centre of Interdisciplinary Plasma Science, Garching, Germany

[†] also: Max Planck Institute for Extraterrestrial Physics, Garching, Germany**Abstract**

In three-dimensional electromagnetic configurations that result from unstable resistive tearing modes particles can efficiently be accelerated to relativistic energies. To prove this resistive magnetohydrodynamic simulations are used as input configurations for successive test particle simulations. The simulations show the capability of three-dimensional non-linearly evolved tearing modes to accelerate particles perpendicular to the plane of the reconnecting magnetic field components. The simulations differ considerably from analytical approaches by involving a realistic three-dimensional electric field with a non-homogenous component parallel to the current direction. The resulting particle spectra exhibit strong pitch-angle anisotropies. Typically, about 5 – 8% of an initially Maxwellian distribution is accelerated to the maximum energy levels given by the macroscopic generalized electric potential structure. Results are shown for both, non-relativistic particle acceleration that is of interest, e.g., in the context of auroral arcs and solar flares, and relativistic particle energization that is relevant, e.g., in the context of active galactic nuclei.

PACS numbers: 52.35.Py – 52.35.Vd – 94.20.Qq – 52.65.Cc

I. INTRODUCTION

Magnetic reconnection is probably the most important mechanism of rapid conversion of magnetic field energy to plasma heating and particle acceleration¹⁻³ in fully and partially ionized plasmas. Cosmic plasma phenomena as different as, e.g., flares in active galactic nuclei⁴(AGN), extragalactic jets^{5,6}, solar flares⁷ and discrete auroral arcs⁸ probably show particle acceleration in reconnection regions.

The problem of particle acceleration is a long standing problem, since the acceleration process depends critically on the local properties of the reconnection region. The efficiency of the particle energization is a function of the effective electric field force that acts on the particle. In two-dimensional reconnection configurations particle acceleration has been extensively studied analytically [e.g., Ref. 9, 10] and numerically within the framework of resistive [e.g., Ref. 11-13] and collisionless [e.g., Ref. 14-16] reconnection. Test particle simulations have proven the efficiency of particle energization in turbulent reconnection [e.g., Ref. 17] These studies have been performed for idealized electric and magnetic field configurations, in particular homogeneous electric fields in the invariant direction, which differ significantly from the three-dimensional configurations characterized by localized field-aligned electric fields.

Test particle simulations of electron injection in high-beta plasmas have shown that the investigation of more complex and therefore more realistic three-dimensional field configurations is crucial for the understanding of particle acceleration in reconnection regions¹⁸. Three-dimensional test particle simulations of particle acceleration in reconnection regions that result from shear flows have proven the short-comings of idealized analytical two-dimensional treatments of the particle acceleration problem¹⁹.

In the present contribution we consider the resistive tearing mode instability, because it is considered as the generic spontaneous reconnection process²⁰ [see also Ref. 2, 3 and references therein]. We present test particle simulations that start from magnetohydrodynamic (MHD) configurations resulting from the non-linear dynamics of tearing modes in three dimensions.

Our studies are relevant for particle acceleration in plasmas that can be described as fluids. Processes that are of importance for particle acceleration in collisionless plasmas as resonant nonlinear wave particle interaction^{21,22} are beyond the scope of our present approach.

The test particle simulations are carried out for different ratios of the asymptotic equilibrium sheared magnetic field component to the field component along the initial current direction. For the initial particle distribution a non-relativistic Maxwellian and a relativistic power law distribution are chosen, respectively. In the next section the initial non-linearly evolved MHD configuration is introduced. In Sec. III the results of the test particle simulations

are presented for the non-relativistic and the relativistic cases. Eventually, we discuss our findings in Sec. IV.

II. THE MHD INITIAL CONFIGURATION

The MHD balance equations that govern the non-relativistic macroscopic low-frequency dynamics read in a dimensionless form

$$\frac{\partial \rho}{\partial t} + \nabla \cdot (\rho \mathbf{v}) = 0 \quad (1)$$

$$\frac{\partial \rho \mathbf{v}}{\partial t} + \nabla \cdot (\rho \mathbf{v} \mathbf{v}) = -\nabla p + \nabla \times \mathbf{B} \times \mathbf{B} \quad (2)$$

$$\frac{\partial p}{\partial t} = -\mathbf{v} \cdot \nabla p - \gamma p \nabla \cdot \mathbf{v} + (\gamma - 1) \eta (\nabla \times \mathbf{B})^2 \quad (3)$$

$$\frac{\partial \mathbf{B}}{\partial t} = \nabla \times (\mathbf{v} \times \mathbf{B}) - \nabla \times (\eta \nabla \times \mathbf{B}) \quad (4)$$

where ρ , \mathbf{v} , p , and \mathbf{B} denote the mass density, bulk velocity, thermal pressure, and the magnetic field. By η the normalized diffusivity, i.e. the inverse magnetic Reynolds number, is denoted. All quantities are made dimensionless by a typical mass density ρ_0 , magnetic field strength B_0 , and length scale L , the Alfvén velocity $v_A = B_0 / \sqrt{4\pi\rho}$ and Alfvénic transit time $t_A = L/v_A$. Other normalizing parameters follow in a generic way.

The balance equations are numerically integrated by means of a three-dimensional finite differences code²³. The MHD simulations start from an initial configuration given by

$$\mathbf{B}^{eq} = B_s \tanh(y) \mathbf{e}_x + B_n \mathbf{e}_z \quad ; \quad \rho^{eq} = \rho_0 \cosh^{-2}(y) \quad (5)$$

which is known as a Harris sheet equilibrium²⁴ with a leading magnetic field component added along the current direction. It is assumed that the ideal gas condition holds $p = nkT$ (where n , T , and k are the particle number density, temperature, and the Boltzmann constant). The resistivity is chosen to be localized around the midplane in the z -direction $\eta = \hat{\eta} \cosh^{-2}((z - 30)/3)$ with an amplitude of $\hat{\eta} = 0.005$. This equilibrium, which can be regarded as an idealized standard current sheet configuration, is perturbed by tearing eigenmodes

$$\begin{aligned} v_x &= \hat{v}_x \rho_0 \sin\left(\frac{\pi x}{x_{\max}}\right) \left(\left(1 - \frac{|y|}{y_{\max}}\right) \left(1 - \frac{|y|}{\eta^{1/4}}\right) - \frac{|y|}{y_{\max}} \right) e^{-\frac{|y|}{\eta^{1/4}}} \\ v_y &= -\hat{v}_y \rho_0 \cos\left(\frac{\pi x}{x_{\max}}\right) \frac{\pi y}{x_{\max}} \left(1 - \frac{|y|}{y_{\max}}\right) e^{-\frac{|y|}{\eta^{1/4}}}. \end{aligned} \quad (6)$$

The simulation runs were performed with the resolution of $77 \times 77 \times 63$ grid points in a numerical box given by $x \in [-25, 25]$, $y \in [-10, 10]$, and $z \in [0, 60]$ in normalized units. In the x - and z -direction an equidistant discretization

was chosen. The highest resolution of the non-equidistant grid in the y -direction is 0.05. The non-linear dynamics of the resistive tearing mode results in a magnetic field configuration with the tearing-like X - and O -point structure in the x - y -plane. The magnetic field used as initial configuration for the first particle test simulations (see Sec. III) is shown in Fig. 1. The respective three-dimensional electric field is shown in Fig. 2. Obviously, a complex three-dimensional electromagnetic field configuration appears which, differs significantly from analytical configurations used to study particle acceleration. We emphasize that our simulations are characterized by non-homogenous magnetic and electric field components perpendicular to the reconnection flows, i.e. along the direction of the initial current sheet. They make an important difference to any analytical approach.

III. SIMULATIONS ON PARTICLE ACCELERATION

Since in many space and astrophysical circumstances unsaturated external shear flows (stellar winds, stellar explosions, jets from quasars, etc...) agitate magnetic fields and drive the resistive tearing modes our MHD calculations are used as the electromagnetic environment for the studies of electron acceleration by means of test particle simulations. We simply want to know how electric particles behave in the complex three-dimensional electro-magnetic field configuration and neglect any back reaction of the particles onto the field structure.

Thus, the electric field is derived only from the MHD quantities \mathbf{B} , \mathbf{v} and η by means of Ohm's law

$$\mathbf{E} = -\frac{1}{c}\mathbf{v} \times \mathbf{B} + \eta \nabla \times \mathbf{B}. \quad (7)$$

Since the data for the electric and magnetic field is only available on a discrete three-dimensional grid the test particle code uses linear interpolation to determine the field values for any location. We note that the term "test particle" simply means that the electromagnetic fields produced by the particles are not changing the global fields, though the effect of synchrotron radiation on the motion of the particles is taken into account, i.e. the relativistic equations of motion have the form

$$\frac{d\mathbf{p}}{dt} = q \left(\mathbf{E} + \frac{1}{\gamma mc} \mathbf{p} \times \mathbf{B} \right) + \mathbf{F}_{Rad}, \quad \frac{d\mathbf{r}}{dt} = \frac{\mathbf{p}}{\gamma m}, \quad (8)$$

where m and q denote the mass and charge of the particles, which are electrons in our case and

$$\gamma = \sqrt{1 + \left(\frac{p}{mc} \right)^2} \quad (9)$$

is the Lorentz factor.

The calculations are relativistic, including the energy losses via synchrotron radiation and inverse Compton scattering by the term \mathbf{F}_{Rad} , which we discuss in detail in Sect. IIIb. For the non-relativistic case of particle acceleration, as considered in the following sub-section, the radiative losses are negligible. The equations are numerically integrated by a Runge-Kutta algorithm of fourth order with an adaptive stepsize control. As a result we get the momentum and location at certain times of each particle in the given ensemble.

IIIa. NON-RELATIVISTIC PARTICLE ACCELERATION

The choice of parameters for our studies of non-relativistic particle acceleration is motivated by the phenomena of discrete auroral arcs for example. Reconnection may play an important role in the energization of auroral particles in Birkeland current sheets^{8,25}. Our results are, however, to be understood as rather general ones for particle acceleration in three-dimensional tearing configurations. Therefore, we present results from test particle simulation runs for three different ratios of B_n to B_s : $B_n/B_s = 1 : 1, 10 : 1$, and $100 : 1$. The strength of the main magnetic field component is chosen as $B_n^{1:1} \approx 10^{-3}$ Gauss. The electric field components are $E_x \approx 10^{-5} B_n$ and $E_y \approx E_z \approx 10^{-4} B_n$, respectively. It is a characteristic feature of 3D reconnection that the magnitude of the electric field component directed along the initial current sheet is of the order of the dominant convective electric field component. The spatial parameters for the first three runs were adjusted to those of auroral phenomena, i.e. the size of the box is $2000 \times 800 \times 2400$ km. The initial position of the particles is uniformly distributed in the $(x, y, 0)$ -plane at the lower z end of the box. For the particle distribution we choose a Maxwellian distribution with a corresponding temperature of $k_B T \approx 1$ eV and a shift of the momentum in the z -direction of a few percent of the thermal energy, thus the distribution is in fact slightly anisotropic. We consider the state when all electrons have left the computational box as the final state.

The trajectories of all electrons for each run are shown in Fig. 3-5 as a projection on the y - z -plane. The gyration motions of the electrons occur on a much smaller scale so that this motion cannot be identified, but it is fully resolved in the simulation. The reconnection zone is placed between $z \approx 1000$ and $z \approx 1500$ where the $\mathbf{E} \times \mathbf{B}$ -drift forces the electrons to move towards the center of the region. Those electrons which start at coordinates with a y -value close to zero are most efficiently accelerated. They leave the box at high z -values while the others leave the box at the x and y boundaries following the magnetic field lines. The acceleration takes place on very short timescales of a few 10^{-1} seconds.

Fig. 6-8 present the initial and final energy spectra of the electrons. Obviously, most of the electrons keep their initial Maxwellian distribution. The injected test-particles are not noticeably heated. Some fraction of the electrons

are accelerated and show a power law with an average index of 1.1 to 1.5. The main recognizable result is the pile-up of electrons at the high energy tail of the distribution, which shows up in all simulations. The heights of the peaks, i.e. the number of accelerated electrons, increase with decreasing B_n/B_s (Fig. 6 to Fig. 8), while the maximum energization is approximately constant.

In Fig. 9-12 the relative momentum distribution of the test particles of the first run is displayed. The $p_x - p_z$ cut of the phase space shows that the accelerated particles have comparable momentum gains in x - and z -direction (Fig. 9-10), whereas there is almost no momentum gain in the y -direction (Fig. 11-12). For the cases with smaller ratios of B_n/B_s the acceleration is almost exclusively along the current sheet.

The pitch angle distribution (Fig. 13) shows a clear anisotropy in the final state, i.e. there is a strong peak of the distribution function at $\cos(\theta) = 1$ along with a depression in between $0 < \cos(\theta) < 0.9$. This might be explained by the fact that the electrons get accelerated by the component of the electric field parallel to the magnetic field, E_{\parallel} . Thus, they only gain momentum parallel to the magnetic field while the perpendicular component p_{\perp} remains constant (just like in the homogeneous case). Consequently, the momentum vector is predominantly directed parallel to the magnetic field. We would like to emphasize that such a pitch angle anisotropy is characteristic for the so-called inverted V events detected by satellites below the main auroral acceleration regions²⁶. Thus, our results corroborate the current striation model for auroral acceleration in which the tearing instability plays a central role⁸.

Fig. 14 shows the initial and final pitch angle distribution for the most energetic particles of the first run with $B_n/B_s = 1 : 1$. This plot clearly indicates that the pitch angles of the most energized particles depend on their initial pitch angle as it is expected for a non stochastic acceleration process.

We emphasize that different from two-dimensional studies²⁷ a significant fraction of the particles is not trapped in the O-point regions and thus efficiently accelerated.

IIIb. RELATIVISTIC PARTICLE ACCELERATION

In this section we discuss simulations in a parameter range which is typical for the central regions of active galactic nuclei. Such objects like quasars are accreting massive black holes surrounded by magnetized accretion disks from which relativistic plasma jets emanate. They exhibit very rapid flares in almost all bands of the electromagnetic spectrum, especially in the TeV-range²⁸. The spectra are power laws, i.e. the radiation is of nonthermal origin, for example synchrotron radiation and/or inverse Compton scattering. The time scales for some these flares are down to 30 min. In other words, within that short time scale a significant number of particles has to be accelerated very

efficiently to provide the observed radiation fluxes. Since we know that these objects contain differentially rotating magnetized gas disks surrounded by magnetized coronae we think that magnetic reconnection may provide the required fast particle acceleration²⁹. As mentioned above the tearing mode is a generic configuration for reconnection, thus we consider acceleration under circumstances typical for the central light year of an active galactic nucleus. We note that our simulations do not consider an individual object or flare event but concentrate on the general mechanism for energetization of relativistic particles in magnetized plasmas. Especially we do not consider the plasma at some specific distance from the central black hole, rather we simulate the part of a plasma volume with a magnetic field typical for the central 10^{18} cm above the magnetized accretion disk and close to the magnetized emanating jet. Accordingly, the size of the computational box was chosen as $(100 \times 40 \times 120) \times 10^{13} \text{ cm}$. The main component of the magnetic field as well as the asymptotic shear component was scaled to $B_n \approx 0.1 \text{ Gauss}$, i.e. the ratio for all relativistic runs was $B_n/B_s = 1 : 1$. The associated electric field reads $E_x \approx 10^{-3}$, $E_y \approx 10^{-2}$, and $E_z \approx 10^{-3}$ in units of B_n .

We show results of three different runs. One run starts with a relativistic Maxwellian distribution (with $kT/mc^2 = 50$) and in the other runs we use initial power law energy distributions for the injected electrons with Lorentz factors ranging from 10^4 up to $2 \cdot 10^6$ and 10^2 up to $2 \cdot 10^4$, respectively. A power law distribution mimics a pre-accelerated electron population in an active galactic nucleus.

In the considered high energy ranges (GeV to TeV) the losses due to synchrotron radiation and inverse Compton scattering certainly play a role, thus the term

$$\begin{aligned} \mathbf{F}_{Rad} \approx & \frac{2}{3} \frac{q^4}{m^2 c^4} \left\{ \mathbf{E} \times \mathbf{B} + \frac{1}{c} \mathbf{B} \times (\mathbf{B} \times \mathbf{v}) + \frac{1}{c} \mathbf{E} (\mathbf{E} \cdot \mathbf{v}) \right\} \\ & - \frac{2}{3} \frac{q^4}{m^2 c^5} \gamma^2 \mathbf{v} \left\{ \frac{16\pi}{3} U_{Ph} + \left(\mathbf{E} + \frac{1}{c} \mathbf{v} \times \mathbf{B} \right)^2 - \frac{1}{c^2} (\mathbf{E} \cdot \mathbf{v})^2 \right\} \end{aligned} \quad (10)$$

now becomes important for the motion of the electrons (see Eq.(8)). Expression (10) is an approximated form of the damping force due to radiation given by Landau and Lifshitz³⁰ which we used in our code. U_{Ph} denotes the photon energy density, which has to be considered for inverse Compton scattering. For AGN coronae a typical value is $U_{Ph} \approx 10^{-4} \text{ erg/cm}^3$.

The resulting synchrotron spectra can be calculated as the sum of total power emitted by each individual electron. The latter is given by³¹

$$P \left(\frac{\omega}{\omega_c} \right) = \frac{\sqrt{3}}{2\pi} \frac{e^3 B}{mc^2} \sin \theta \frac{\omega}{\omega_c} \int_{\frac{\omega}{\omega_c}}^{\infty} K_{\frac{5}{3}}(\xi) d\xi, \quad (11)$$

where ω_c is the critical frequency, θ is the pitch angle and $K_{\frac{5}{3}}$ is the modified Bessel function.

Let us first discuss the case with an initial power law with an energy range from $\gamma = 10^4 - 2 \cdot 10^6$. The initial and final energy spectra are presented in Fig. 15. Quite a large fraction of the electrons get decelerated below $\gamma \sim 10^4$ whereas some reach energies up to $\gamma \sim 10^7$. The deceleration of particles is caused by the electromagnetic forces and associated radiation losses they experience along their trajectories. Different from the accelerated particles they do not enter the inner reconnection region where the dominant electric field component is directed parallel to their guiding center motion. Their enhanced perpendicular momentum gives rise to efficient radiative losses.

The distribution also shows this beam-like built-up of electrons at higher energies which was observed in the low energy simulations. Unlike the non-relativistic simulations, here the electrons get somewhat decelerated after leaving the reconnection region due to the radiation losses, but still have much higher energies in the end than before.

The deceleration of electrons is also visible in the radiation spectrum of the synchrotron emission since the initial spectrum, or radiation power distribution, reaches up to higher frequencies than the final spectrum (Fig. 16). On the other hand, the accelerated particles ($\gamma > 10^6$) have a very small pitch angle and therefore do not significantly contribute to the synchrotron emission within our simulation volume. Interesting enough such an anisotropic particle distribution is able to transport energy to regions far away from the acceleration site, since the particles do not lose energy by synchrotron radiation. Such a behavior has been demanded by Ghisellini³² for the X-ray and gamma-ray bursting blazars. There must be some energy transport mechanism which is dissipationless up to large distances from the acceleration site, and the appearance of an anisotropic ultrahigh energy component would present such a mechanism³³.

The selection which electrons are to be accelerated or decelerated is certainly due to a geometric effect, i.e. only those electrons which have an appropriate initial position experience a strong acceleration. This is visible in Fig. 17-21 in which the trajectories of these two classes of particles are presented. Obviously, only those electrons are most efficiently accelerated which are injected very close to the quasi-separatrix layers. The separatrix-like projection onto the x - y -plane does not necessarily indicate regions of different magnetic topology in the considered three-dimensional configuration. The trajectories of accelerated and decelerated particles are somehow complementary to each other. An interesting feature is the sickle-shaped form of the trajectories in the z - y -projection. It seems as if the reconnection zone acts like a defocusing lens to the accelerated electrons. The decelerated electrons do not move along reconnecting magnetic field lines that cross the initial neutral layer.

In the second run, initialized with an energy range from $\gamma = 10^2 - 2 \cdot 10^4$, the energy and synchrotron spectra are

shown in Fig. 22 and 23. The pile-up at $\gamma \sim 8 \cdot 10^6$ is less pronounced, but still present. The radiation spectrum clearly exhibits a broken power law. The low energy part of the power law is mainly due to the initially injected particles, whereas the high energy part is caused by the accelerated particle population. The particle trajectories are qualitatively similar to the previously discussed run. The same statement holds for the case of the initial relativistic Maxwellian particle distribution. For this case also efficient acceleration occurs (Fig. 24, 25) but there is no pile-up at high energies. The radiation exhibits a rather flat spectrum at higher energies. This is of particular interest in the context of observations indicating flat nonthermal spectra of blazars^{34,35} like Mrk 421 and Mrk 501.

IV. DISCUSSION

Particle acceleration in magnetized collisionless plasmas is a central issue of high energy astrophysics and space physics. A large number of observation in all bands of the electromagnetic spectrum demand for a fast and efficient production of accelerated particles within magnetized plasmas which are agitated by unsaturated external forces like differential rotation, jets, stellar winds and explosive events. Such forces twist, shear and stretch field lines into configurations in which magnetic reconnection plays a dominant role either as relaxation mechanisms and/or as acceleration process. The tearing instability is known to be a generic configuration in such reconnection sites.

Thus, we studied the acceleration of non-relativistic and relativistic electron populations in three-dimensional tearing configurations. By means of test particle simulations performed within non-linearly evolved electromagnetic fields modeled by MHD simulations we could show that particles are effectively accelerated. Our simulations include nonthermal radiative losses like synchrotron radiation. Starting from a shifted Maxwellian distribution we carried out test particle simulations for three different ratios of the magnitudes of the initial magnetic field components parallel and perpendicular to the current sheet. For example, we have chosen physical parameters that are relevant for auroral acceleration zones. Our findings are, however, of general interest for particle acceleration in reconnecting current sheets. The degree of the pitch angle anisotropy of the accelerated particles depends on the strength of the guiding magnetic field component along the current sheet. A significant fraction of the initially injected electrons gains momentum. The level of energization is limited by the overall generalized electric potential $U = \int ds E_{||}$.

The relativistic studies dealt with the fate of electrons that enter the reconnection region with a power law distribution. Such a situation is characteristic for flares in active galactic nuclei. Some fraction of the pre-accelerated particles is fast and efficiently energized in the three-dimensional tearing configuration. As in the runs that start from a Maxwellian distribution a high-energy bump forms in the final distribution.

Our simulations prove the capability of magnetic reconnection to energize an electron population of a magnetized plasma under the influence of external electromagnetic fields onto which the accelerated leptons have no back reaction. For example, close to a black hole the differential rotation of the surrounding accretion disk which shears magnetic field lines is only determined by the mass of a central object but not influenced by the dissipation of magnetic energy in small current sheets. In other words, the external forces which stretch, fold and twist the magnetic field lines act on a much larger spatial scale than the size of the forming current sheets. This behavior is similar to what is known from turbulent plasmas, in which the energy input on large spatial scales is finally dissipated on considerably smaller length scales. Thus, the energy sources and energy sinks are completely disconnected from each other. Furthermore, the enormous strength of such global forces like differential rotation substantiates our test particle approach, which implicitly assumes no back reaction of the particles onto the electrodynamic structure of the plasma.

Our present studies do not include turbulent electromagnetic fields. Numerical studies of particle acceleration in MHD turbulent reconnection regions seem to be a promising task for the future.

REFERENCES

- [1] R.D. Bentley and J.T. Mariska (eds.), *Magnetic Reconnection in the Solar Atmosphere*, ASP Conf. Ser. **111** (1996).
- [2] E.R. Priest and T. Forbes, *Magnetic reconnection: MHD theory and applications* (Cambridge University Press, New York, 2000).
- [3] D. Biskamp, *Magnetic Reconnection in Plasmas* (Cambridge University Press, Cambridge, 2000).
- [4] H. Lesch and G.T. Birk, *Astron. Astrophys.* **324**, 461 (1997).
- [5] E.G. Blackman, *Astrophys. J.* **456**, L87 (1996).
- [6] H. Lesch and G.T. Birk, *Astrophys. J.* **499** 167 (1998).
- [7] E.R. Priest and T. Forbes, *Astron. Astrophys. Rev.* **10**, 313 (2000).
- [8] A. Otto and G.T. Birk, *Geophys. Res. Lett.* **20**, 2833 (1993).
- [9] J.S. Wagner, P.C. Gray, J.R. Kan, T. Tajima, and S.-I. Akasofu, *Planet. Space Sci.* **4**, 391 (1981).
- [10] Y. Litvinenko, *Astrophys. J.* **462**, 997 (1996).
- [11] D.L. Bruhwiler and E.G. Zweibel, *J. Geophys. Res.* **97**, 10825 (1992).
- [12] W. Moses, J.M. Finn, and K.M. Ling, *J. Geophys. Res.* **98**, 4013 (1993)
- [13] B. Kliem, *Astrophys. J. Supp.* **90**, 719 (1994).
- [14] R. Horiuchi and T. Sato, *Phys. Plasma* **4**, 277 (1997).
- [15] G.E. Vekstein and P.K. Browning, *Phys. Plasma* **4**, 2261 (1997).
- [16] Y.E. Litvinenko, *Phys. Plasma* **4**, 3439 (1997).
- [17] J. Ambrosiano, W.H. Mattheus, M.L. Goldstein and D. Plante, *J. Geophys. Res.* **93**, 14383 (1988).
- [18] J. Birn, M.F. Thomsen, J.E. Borovsky, G.D. Reeves, D.J. McComas and R.D. Belian, *J. Geophys. Res.* **103**, 9235 (1998).

[19] R. Schopper, G.T. Birk, and H. Lesch, *Phys. Plasmas* **6**, 4318 (1999).

[20] H.P. Furth, J. Killeen, and M.N. Rosenbluth, *Phys. Fluids* **6**, 459 (1963).

[21] M. Hoshino, J. Arons, Y. A. Gallant, A. B. Langdon, *Astrophys. J.* **390**, 454 (1992).

[22] D. B. Melrose, in *Plasma Astrophysics*, eds. J. G. Kirk, D. B. Melrose, and E. R. Priest (Springer, Berlin, 1994) p. 113.

[23] A. Otto, *Comp. Phys. Com.* **59**, 185, (1990).

[24] E.G. Harris, *Nuovo Cimento* **23**, 115 (1962).

[25] G.T. Birk and A. Otto, *J. Atm. Sol.-Terr. Phys.*, **59**, 835, (1997).

[26] C.S. Lin and R.A. Hoffmann, *J. Geophys. Res.*, **84**, 1514 (1979).

[27] J.S. Wagner, J.R. Kan and S.-I. Akasofu, *J. Geophys. Res.*, **84**, 891, (1979).

[28] J.A. Gaidos, C.W. Akerlof, S.D. Biller *et al.*, *Nature*, **383**, 319 (1996).

[29] H. Lesch, *Plasmas in the Universe*, eds. B. Coppi, A. Ferrari, E. Sinodi (IOS Press, Amsterdam, 2000) p. 395.

[30] L. D. Landau and E. M. Lifshitz, *The Classical Theory of Fields* (Addison-Wesley, Reading MA., 1951).

[31] G. B. Rybicki and A. P. Lightman, *Radiative Processes in Astrophysics* (Wiley, New York, 1979) ch. 6.2.

[32] G. Ghisellini, *BL Lac Phenomena*, Astronomical Society of the Pacific, 159, 311 (1999).

[33] A. Crusius-Wätzel and H. Lesch, *Astron. Astrophys.*, 299, 404 (1998).

[34] G. Tosti, *et al.*, *Astron. Astrophys.*, 339, 41 (1998).

[35] P. G. Edwards, G. Giovannini, W. D. Cotton, L. Feretti, K. Fujisawa, H. Hirabayashi, L. Lara, and T. Venturi, *Publ. Astron. Soc. Japan*, 52, 1015 (2000).

FIGURE CAPTIONS

Figure 1: The magnetic field configuration that results from the MHD simulation after 180 Alfvén times. The upper plot shows magnetic field lines, the lower one shows an arrow plot of the x - and y -components of the magnetic field at $z = 30$.

Figure 2: The electric field configuration after $t = 180\tau_A$. The upper plot shows electric field lines, the lower one shows an arrow plot of the y - and z -components of the electric field at $x = 3$.

Figure 3: The trajectories of all electrons of the first run ($B_n/B_s = 1 : 1$) as a projection on the $y - z$ plane.

Figure 4: The trajectories of all electrons of the second run ($B_n/B_s = 10 : 1$) as a projection on the $y - z$ plane.

Figure 5: The trajectories of all electrons of the third run ($B_n/B_s = 100 : 1$) as a projection on the $y - z$ plane.

Figure 6: The spectrum of kinetic energy in the first run. The relative number frequency is plotted against the kinetic energy in units of mc^2 . The dotted line represents the initial distribution while the normal line is the final distribution.

Figure 7: The spectrum of kinetic energy in the second run.

Figure 8: The spectrum of kinetic energy in the third run.

Figure 9: The initial momentum plotted in the $p_x - p_z$ plane of phase space of the first run ($B_n/B_s = 1 : 1$).

Figure 10: The gain of momentum in z direction compared to that in x direction. For most of the accelerated particles p_z is only slightly higher than p_x .

Figure 11: The initial momentum plotted in the $p_y - p_z$ plane of phase space of the first run ($B_n/B_s = 1 : 1$).

Figure 12: The gain of momentum in z direction compared to that in y direction. There is no noticeable gain in y direction.

Figure 13: The pitch angle distribution at the beginning (dotted line) and at the end (normal line) of the first simulation ($B_n/B_s = 1 : 1$). The relative number frequency is plotted against $\cos(\theta)$.

Figure 14: The pitch angle distribution of the electrons with the highest energy gain. These electrons already start with very small pitch angles.

Figure 15: The energy spectrum of the first relativistic run. This simulation started with a power law (dotted line) of $N(\gamma - 1)d\gamma = (\gamma - 1)^{-2}d\gamma$. The final spectrum (normal line) shows a local maximum at ($\gamma - 1 \sim 8 \times 10^6$).

Figure 16: The synchrotron spectrum of the first relativistic run.

Figure 17: The trajectories of the relativistic run as a projection on the $y - z$ plane.

Figure 18: The trajectories of the accelerated electrons as projection on the $y - z$ plane.

Figure 19: The trajectories of the decelerated electrons as projection on the $y - z$ plane.

Figure 20: The trajectories of the accelerated electrons as projection on the $x - y$ plane.

Figure 21: The trajectories of the decelerated electrons as projection on the $x - y$ plane.

Figure 22: The energy spectrum of the second relativistic run. This simulation started with a power law (dotted line) of $N(\gamma - 1)d\gamma = (\gamma - 1)^{-2}d\gamma$. The final spectrum (normal line) shows a pile-up at ($\gamma - 1 \sim 8 \times 10^6$).

Figure 23: The synchrotron spectrum of the second relativistic run.

Figure 24: The energy spectrum of the third relativistic run that started with a power law (dotted line) of $N(\gamma - 1)d\gamma = (\gamma - 1)^{-2}d\gamma$.

Figure 25: The synchrotron spectrum of the third relativistic run.

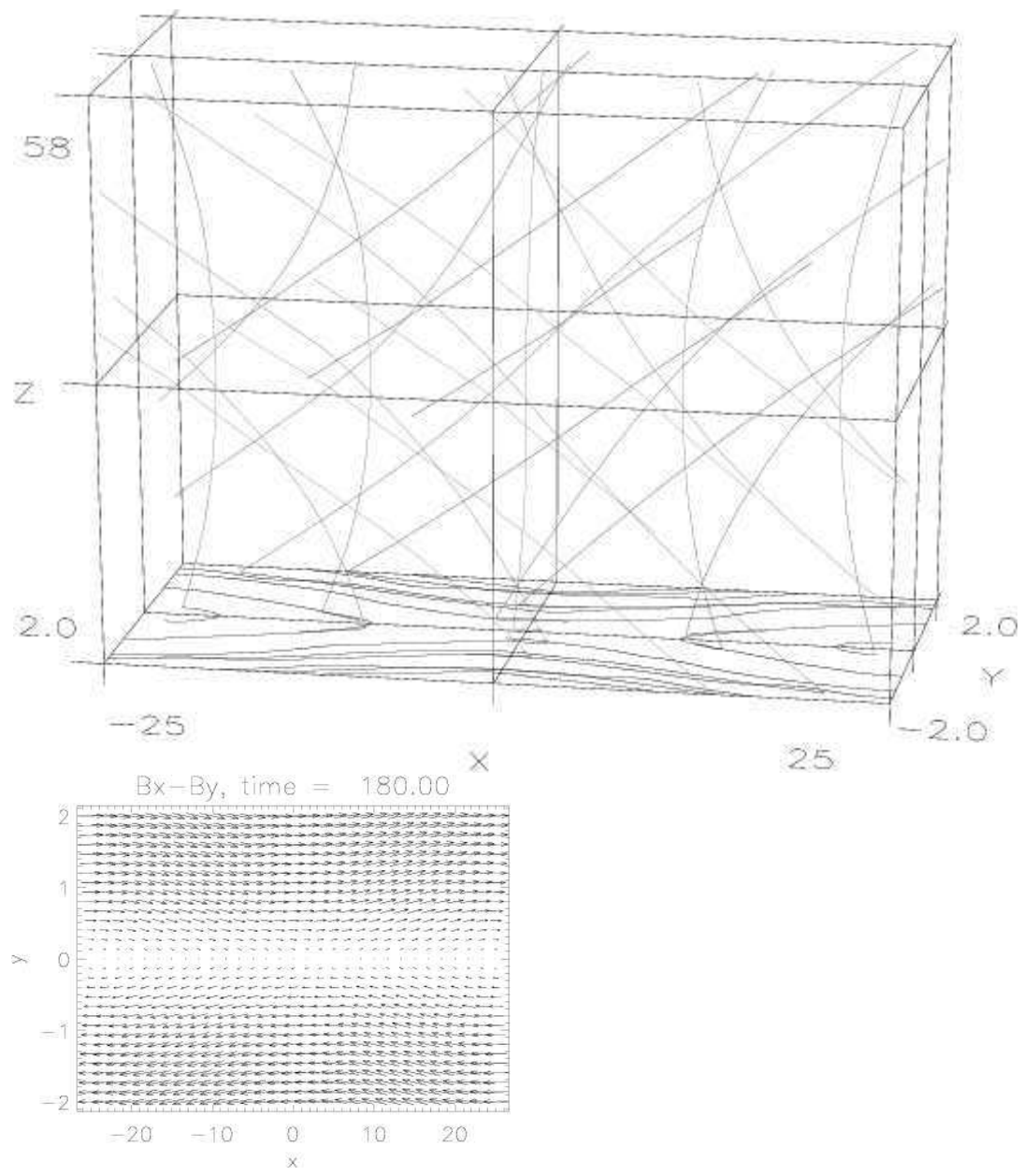
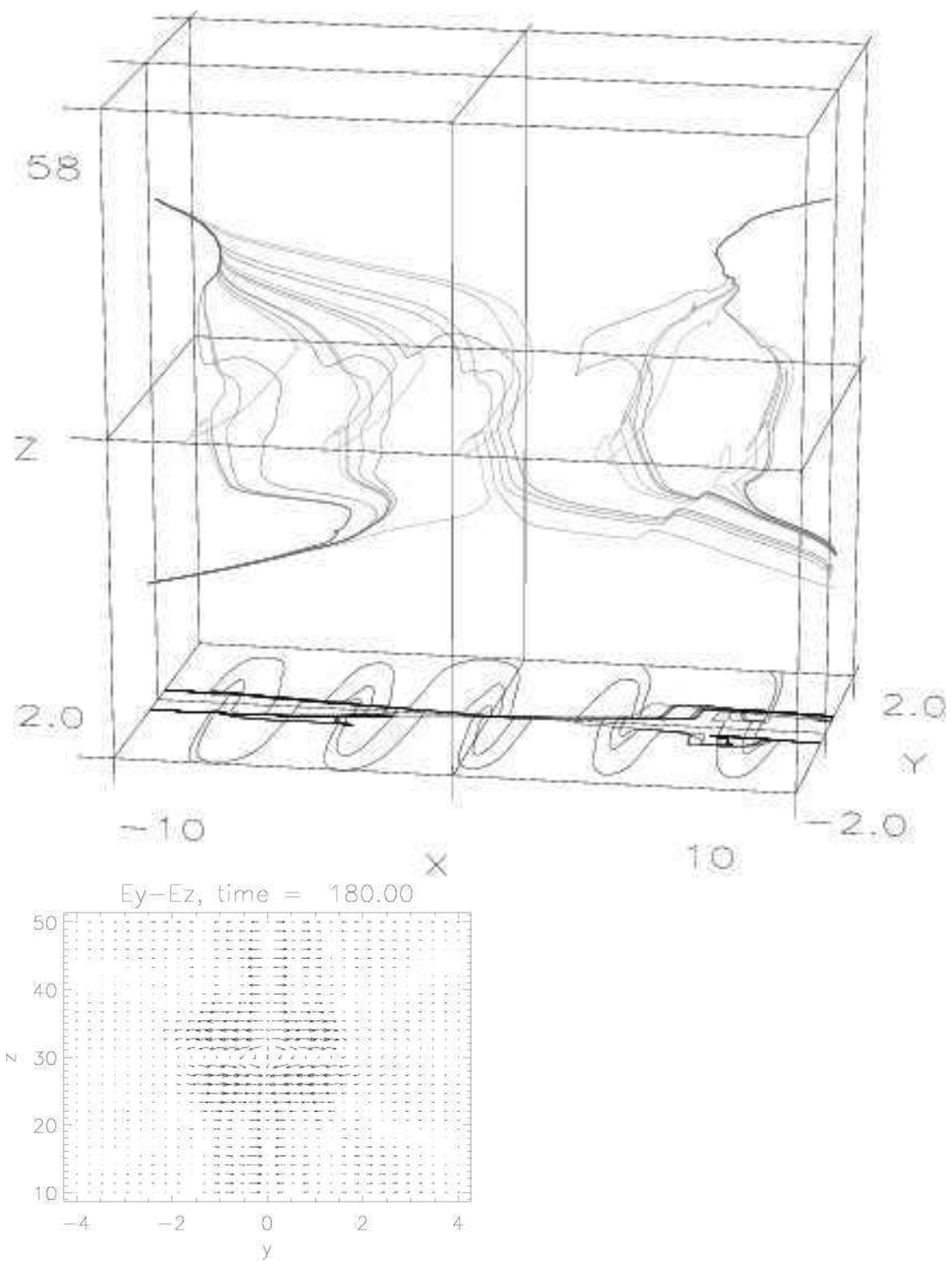


Fig. 1.



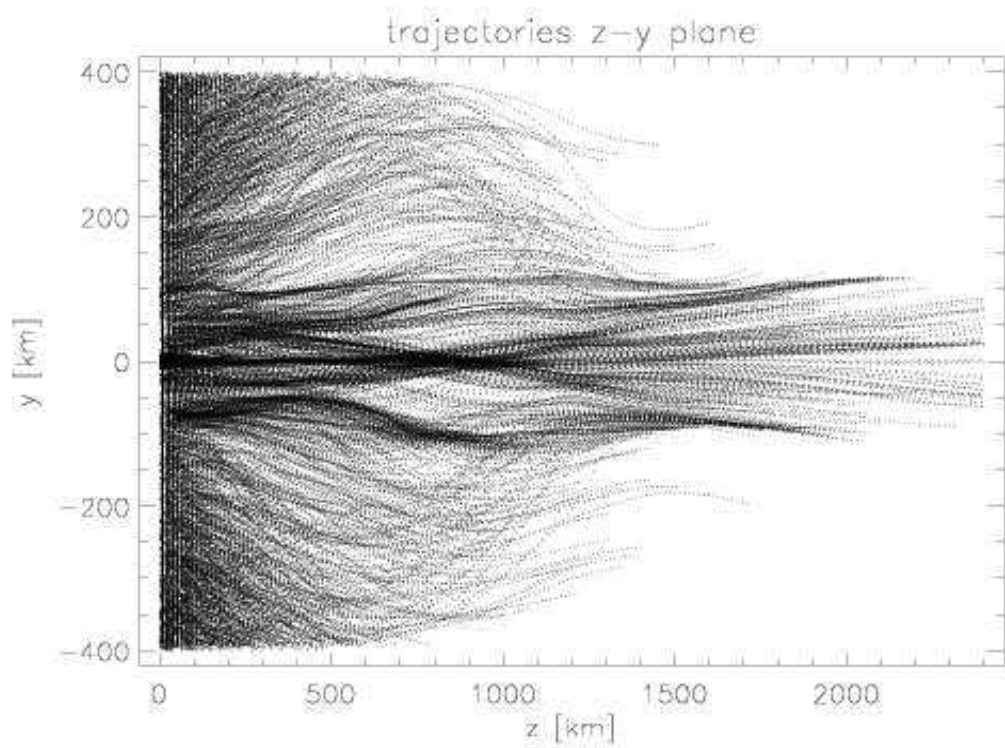


Fig. 3.

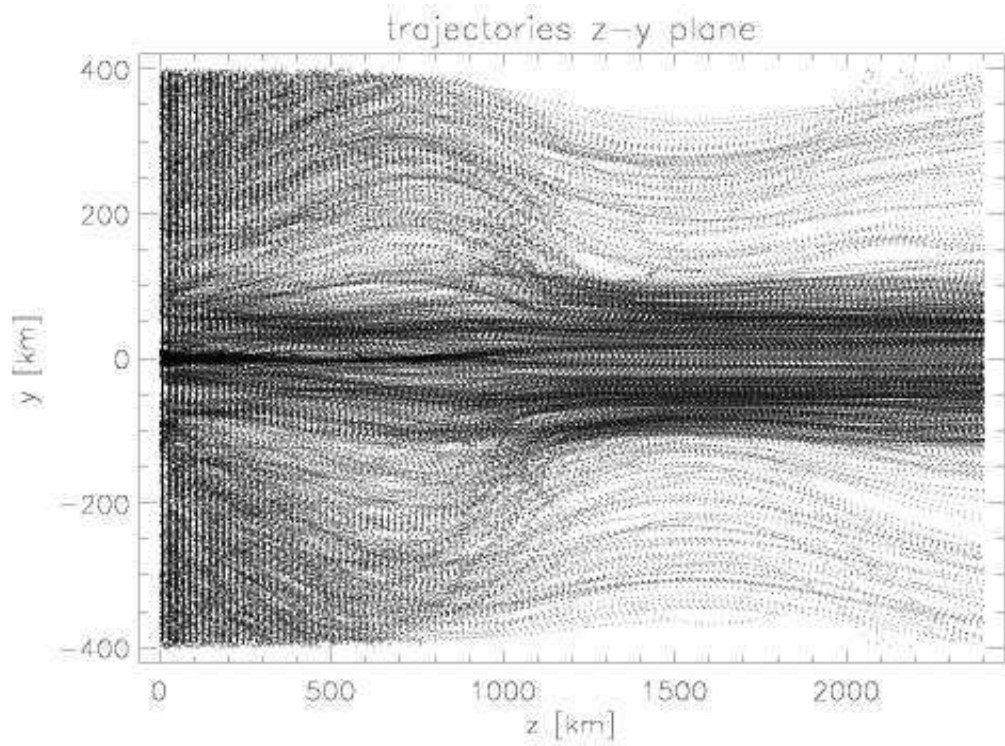


Fig. 4.

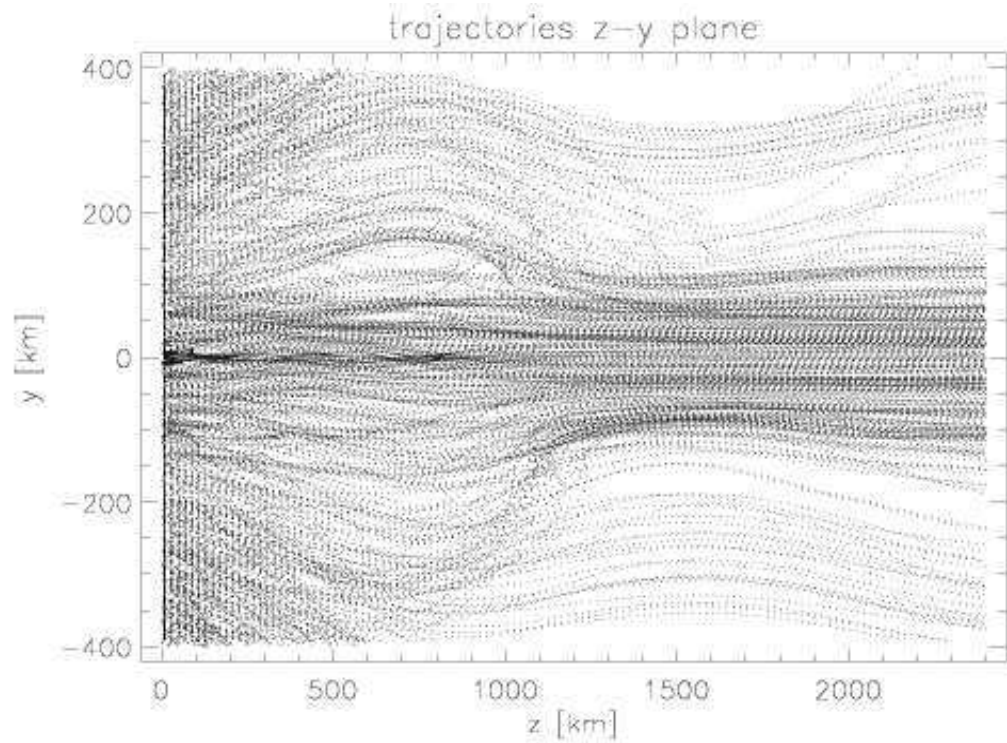


Fig. 5.

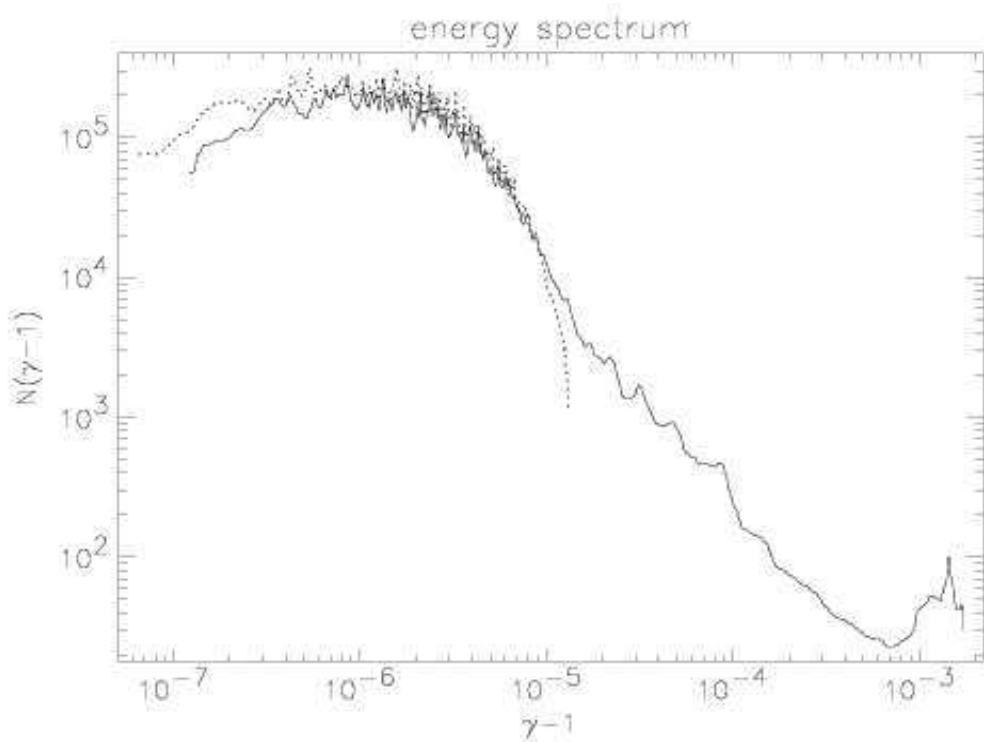


Fig. 6.

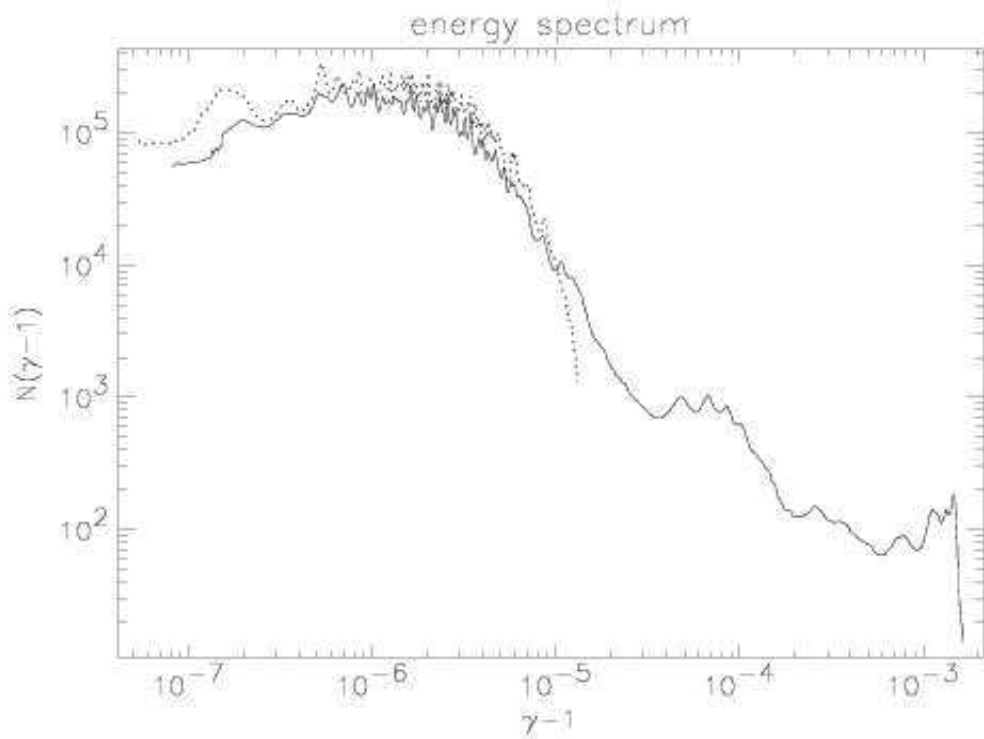


Fig. 7.

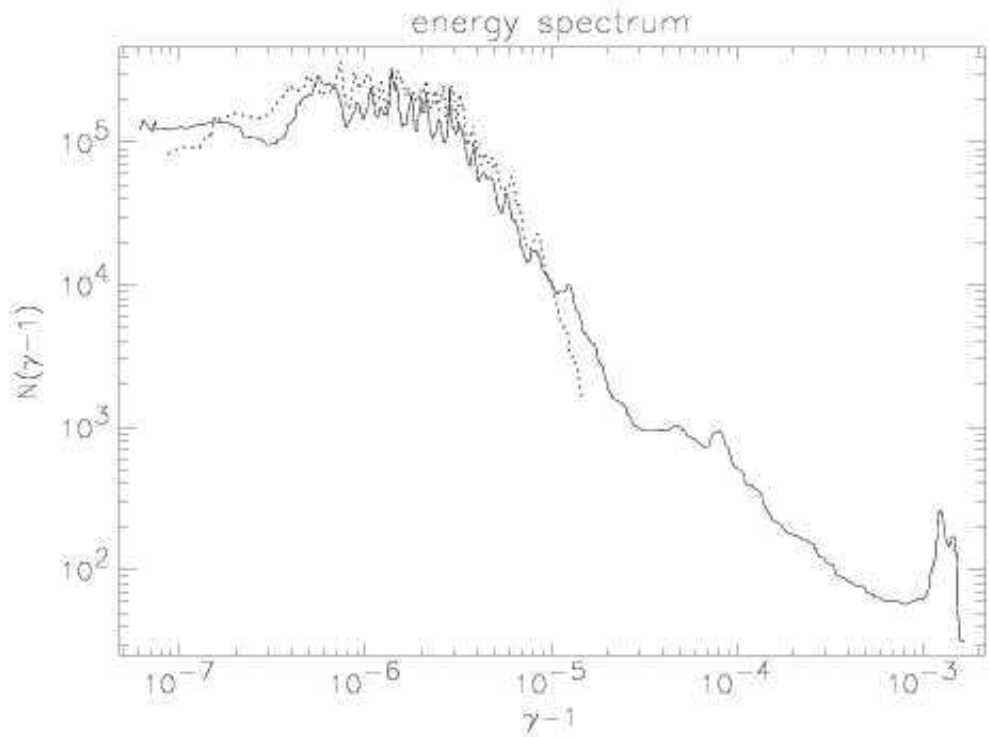


Fig. 8.

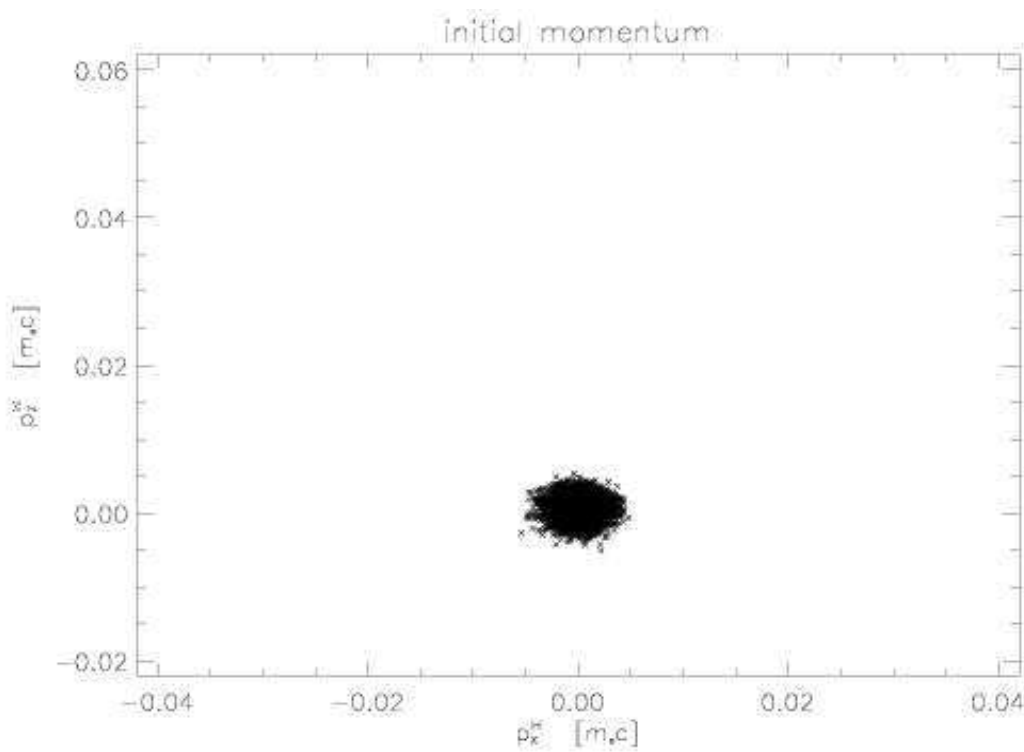


Fig. 9.

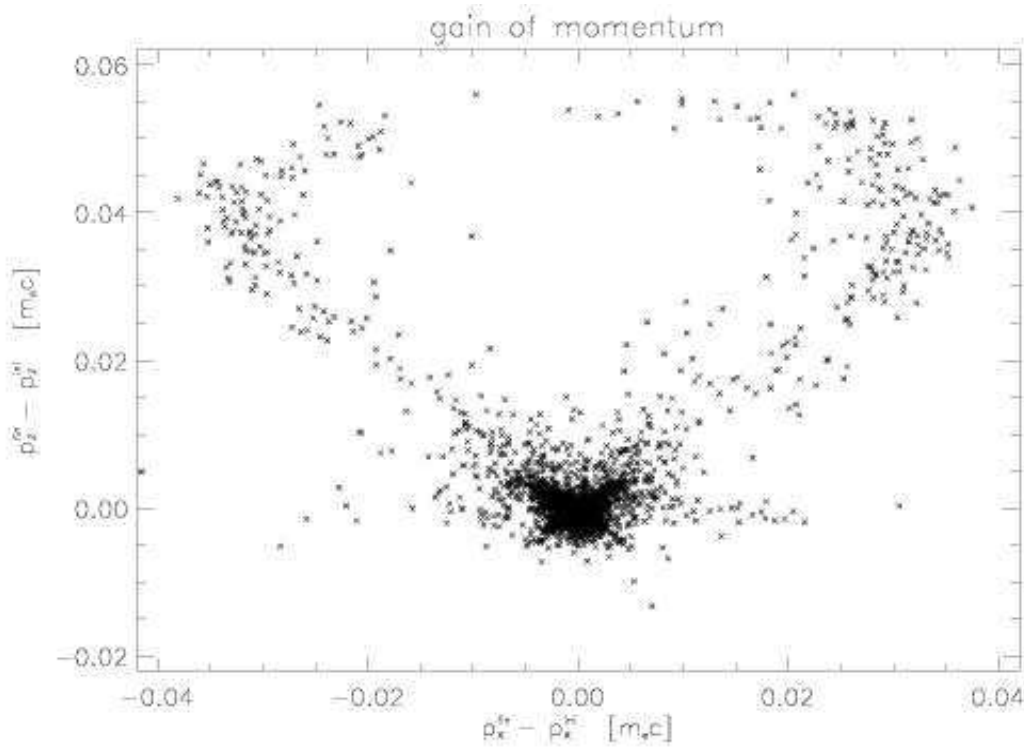


Fig. 10.

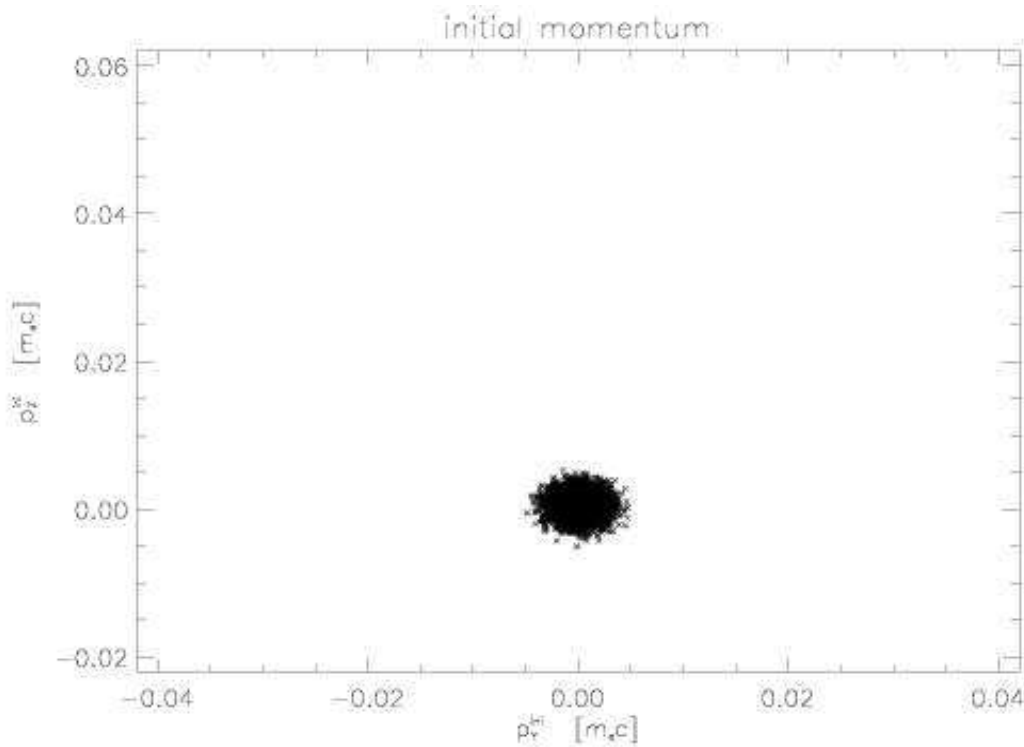


Fig. 11.

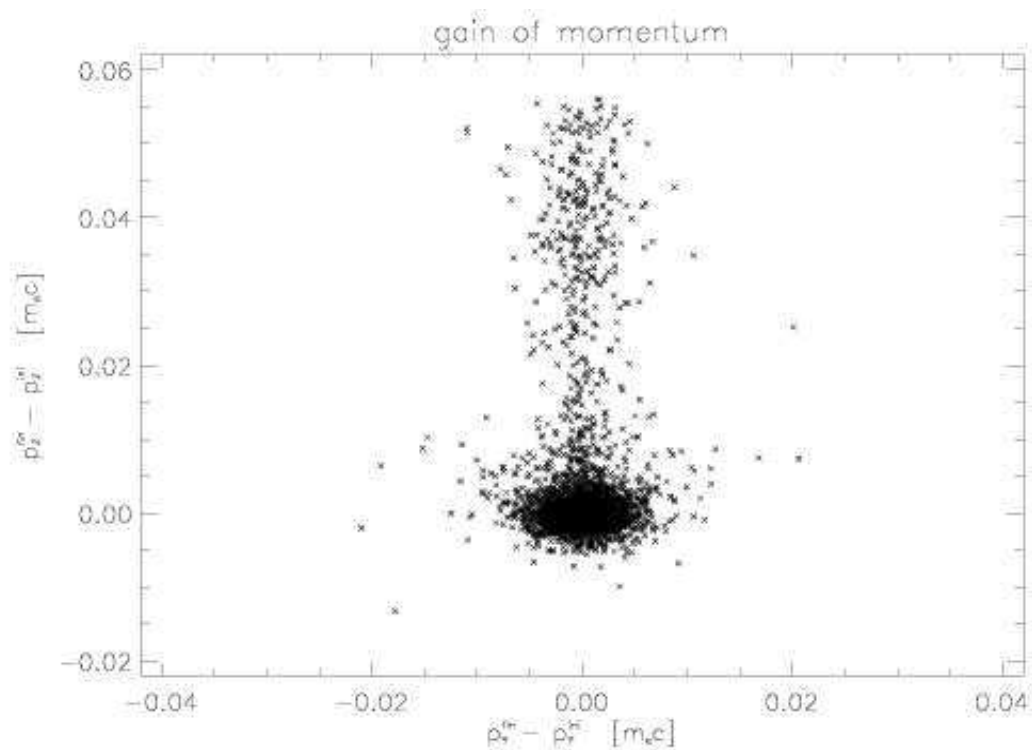


Fig. 12.

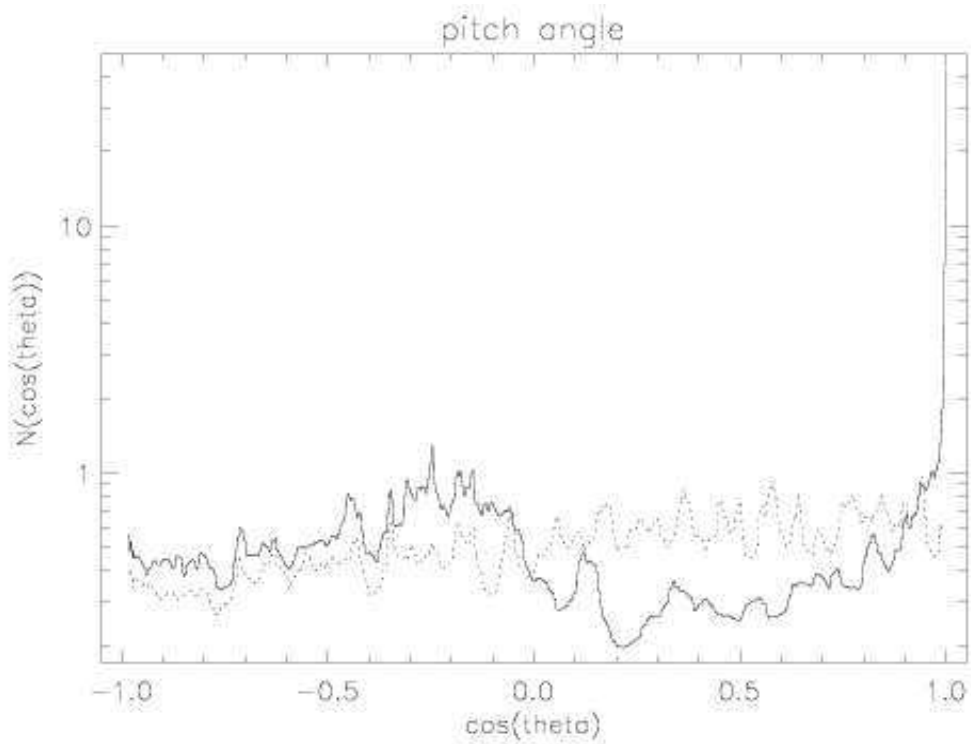


Fig. 13.

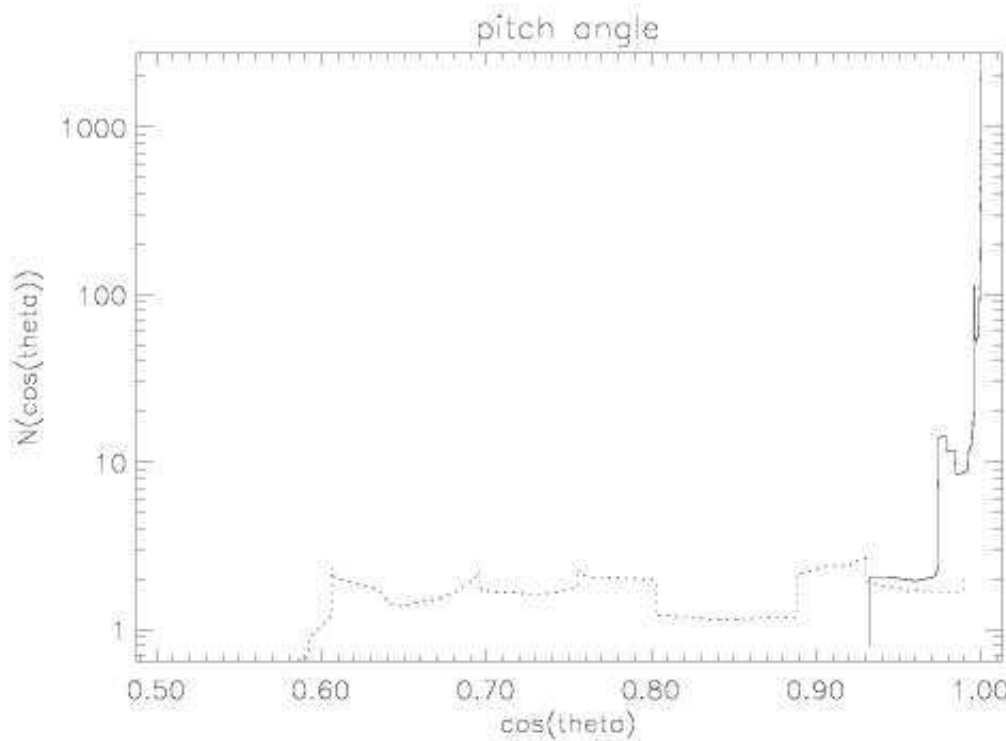


Fig. 14.

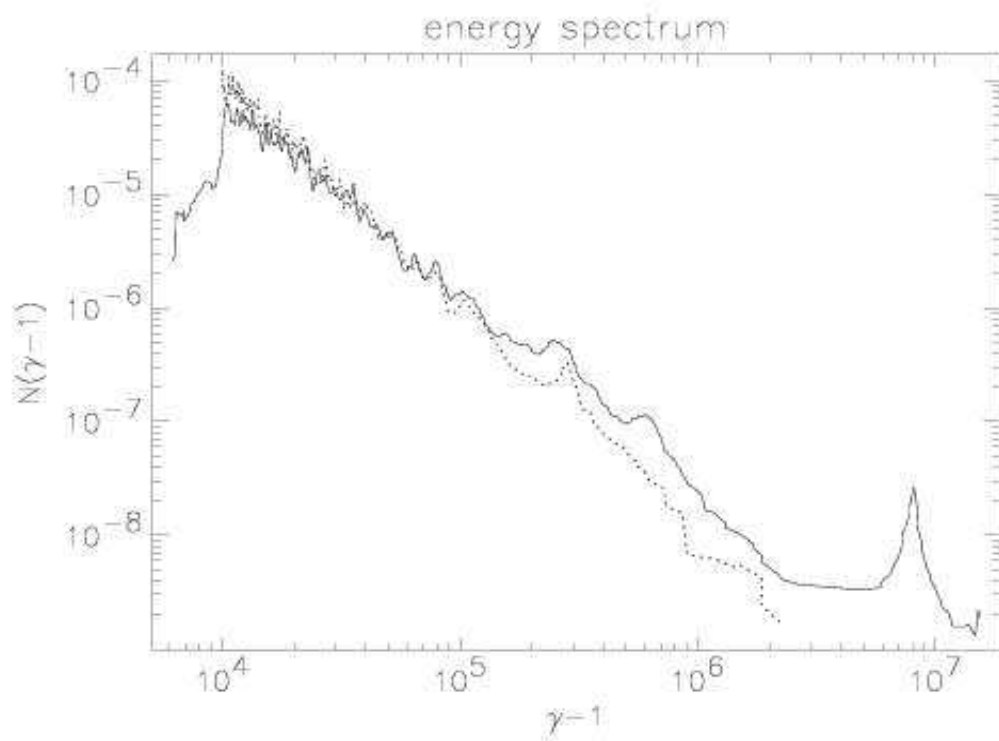


Fig. 15.

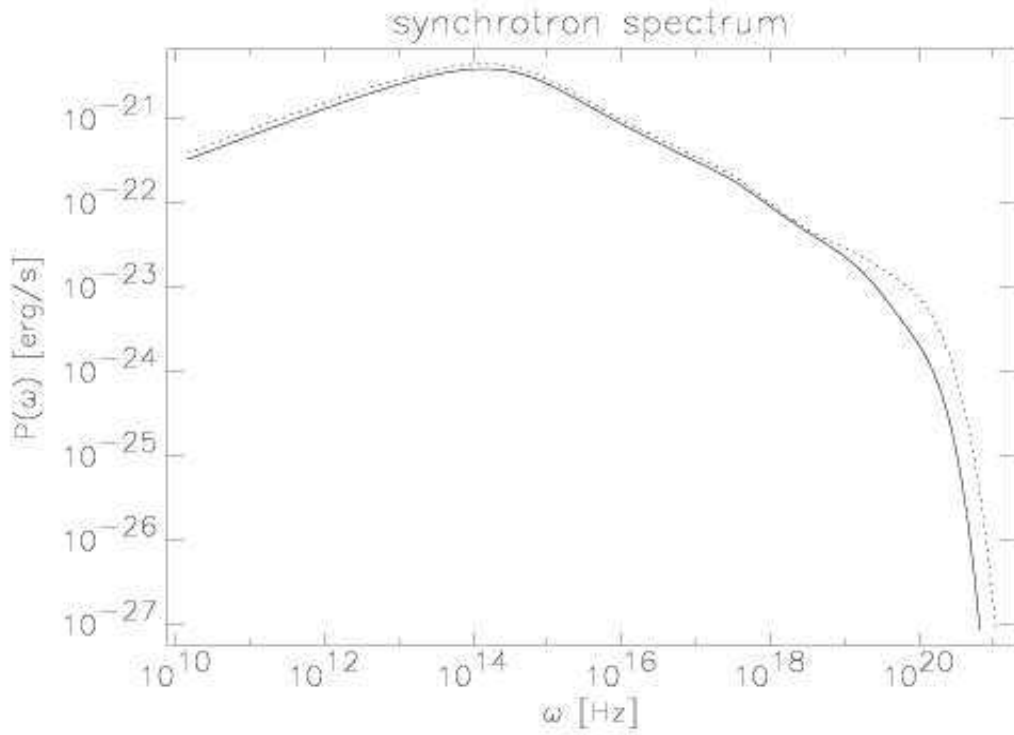


Fig. 16.

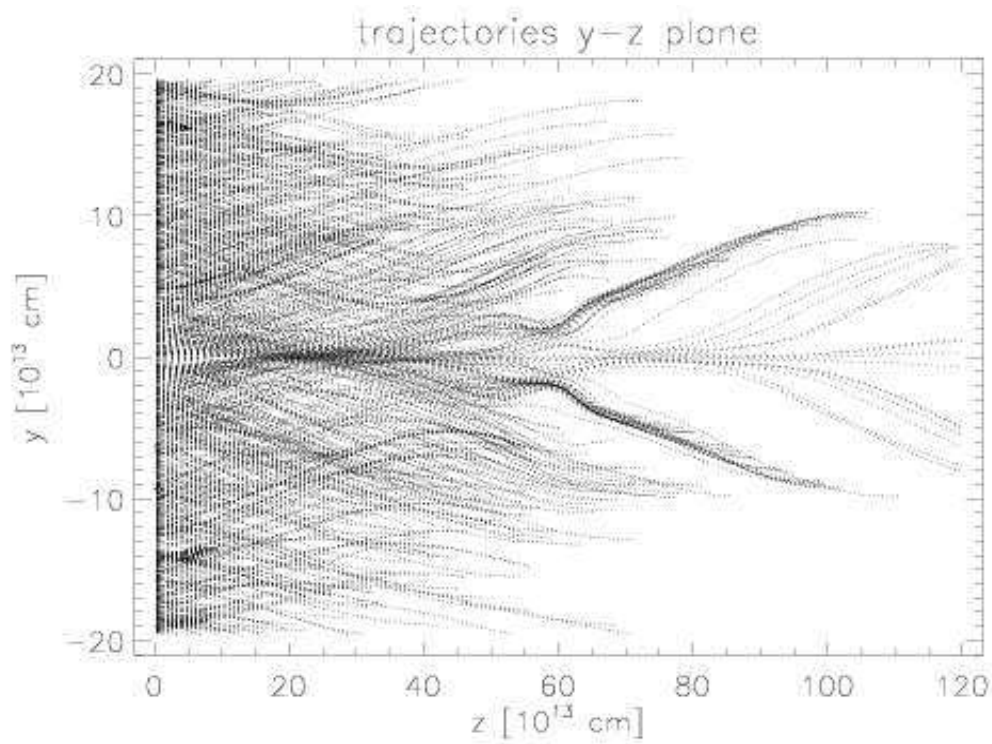


Fig. 17.

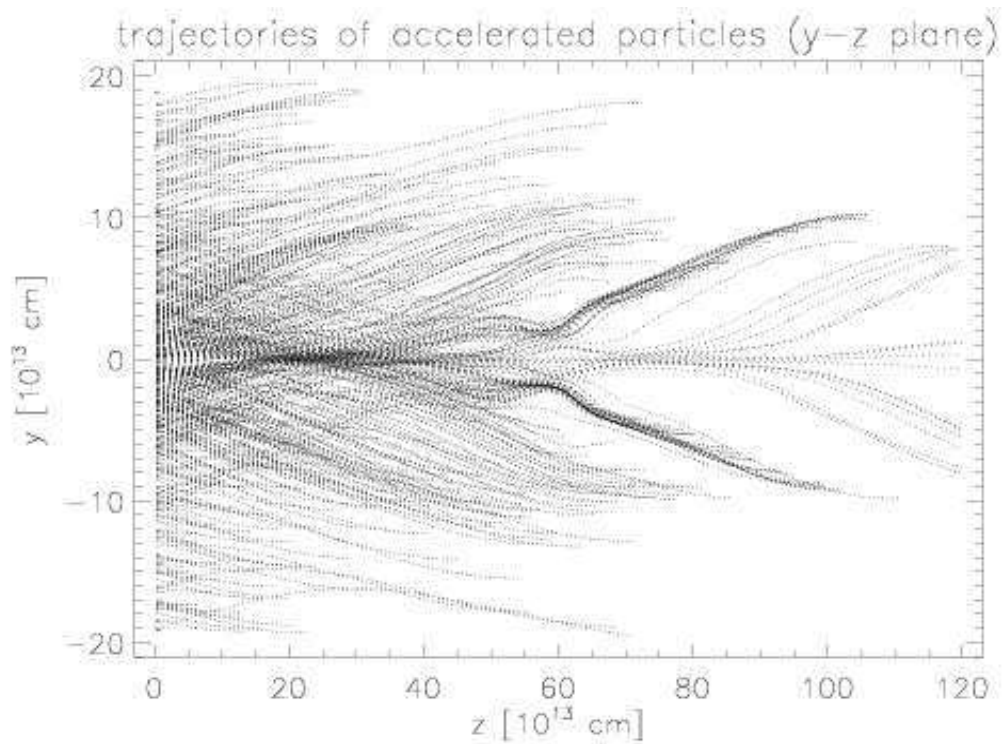


Fig. 18.

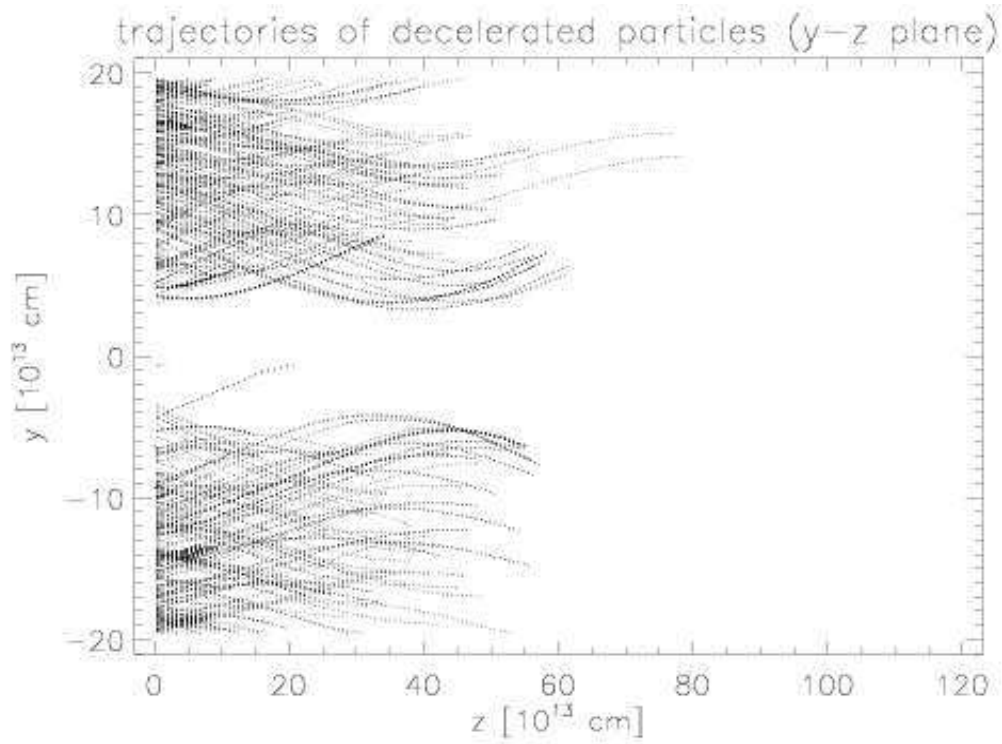


Fig. 19.

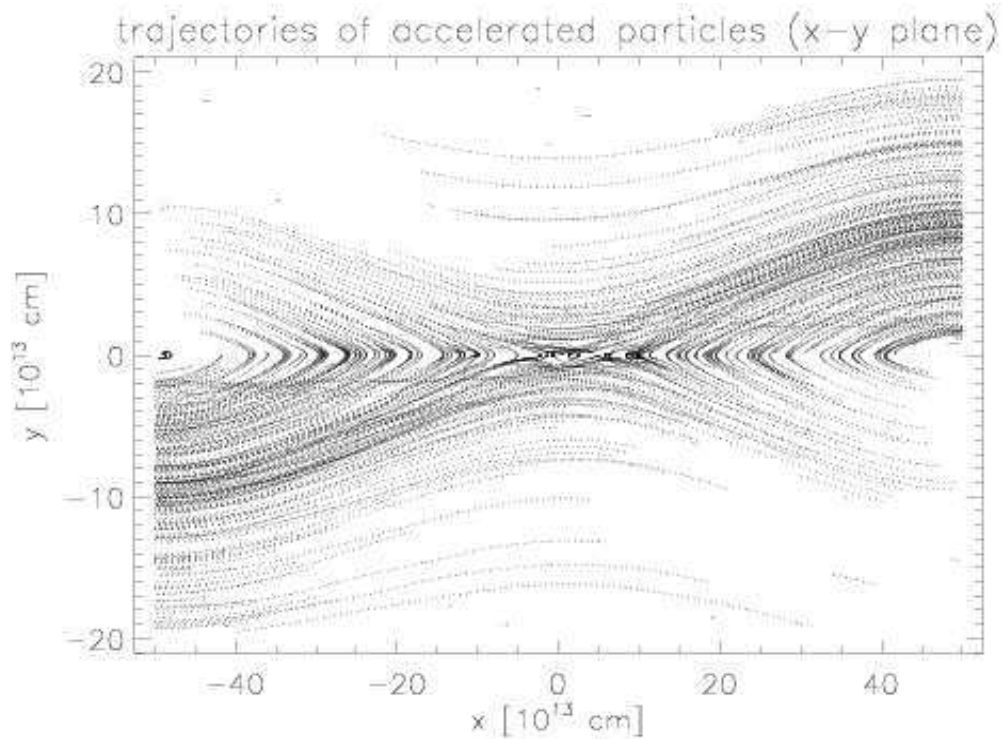


Fig. 20.

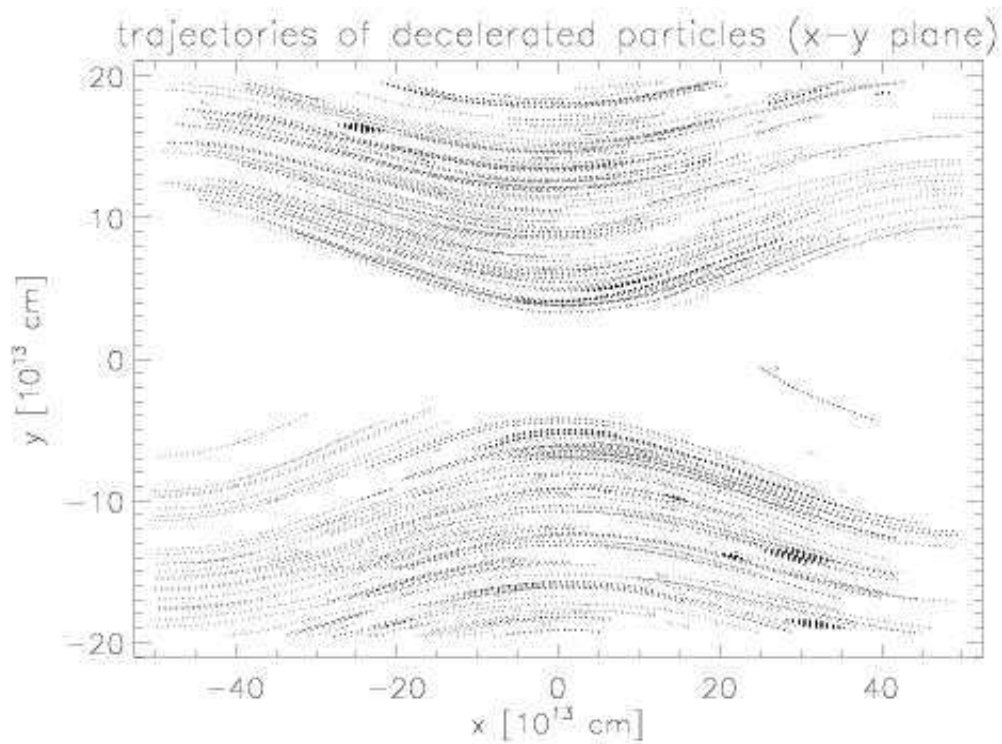


Fig. 21.

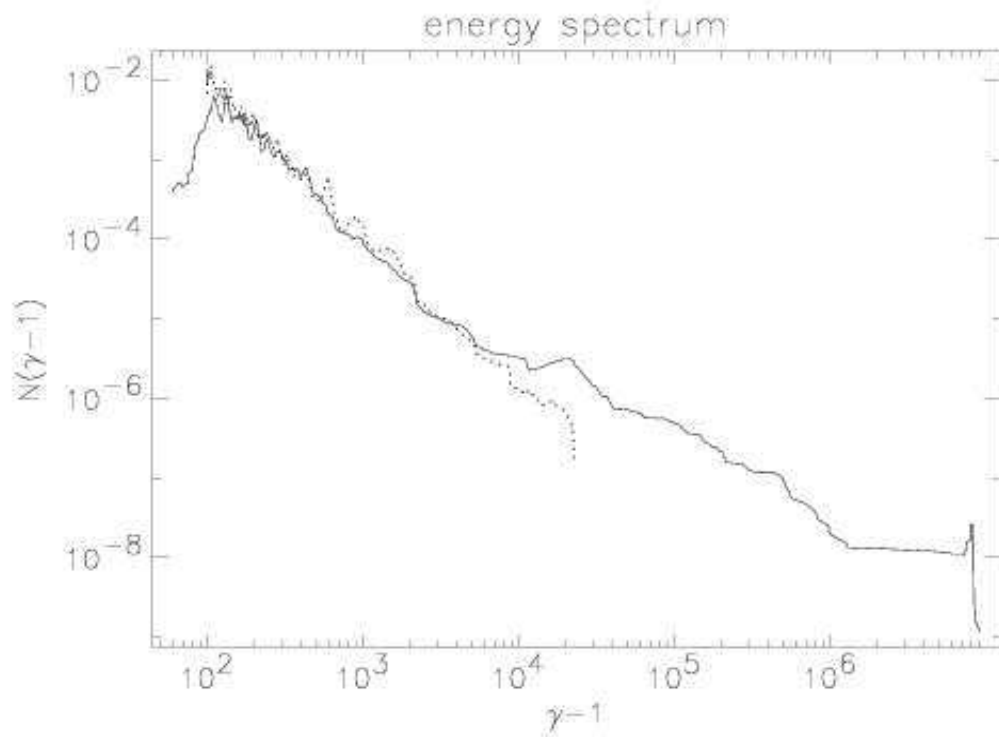


Fig. 22.

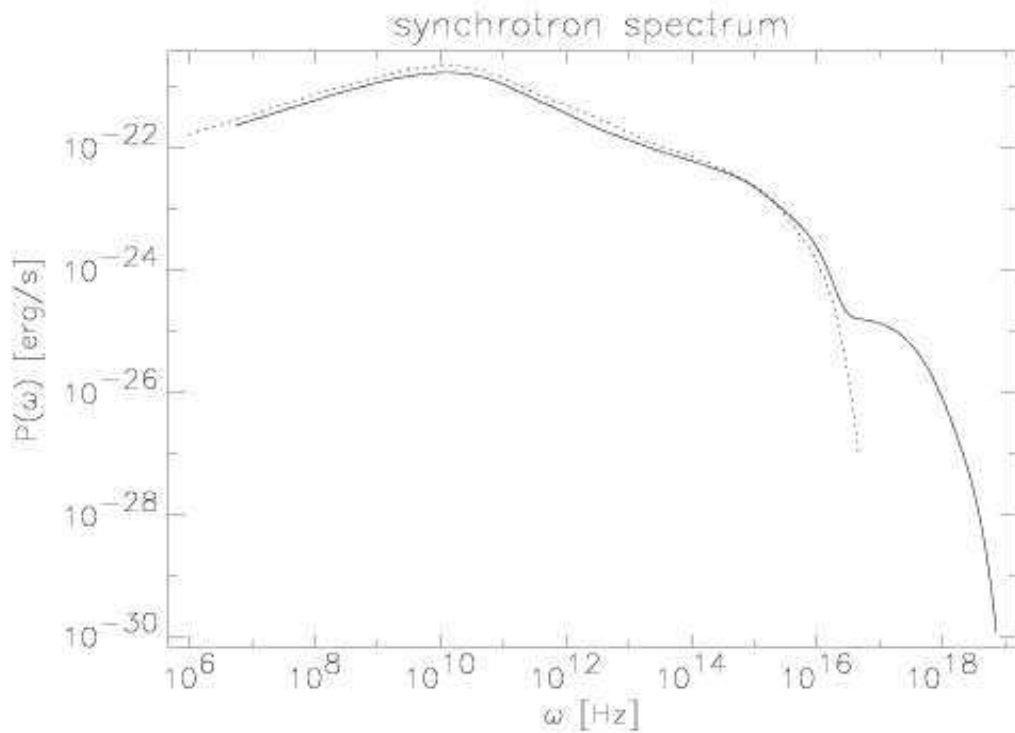


Fig. 23.

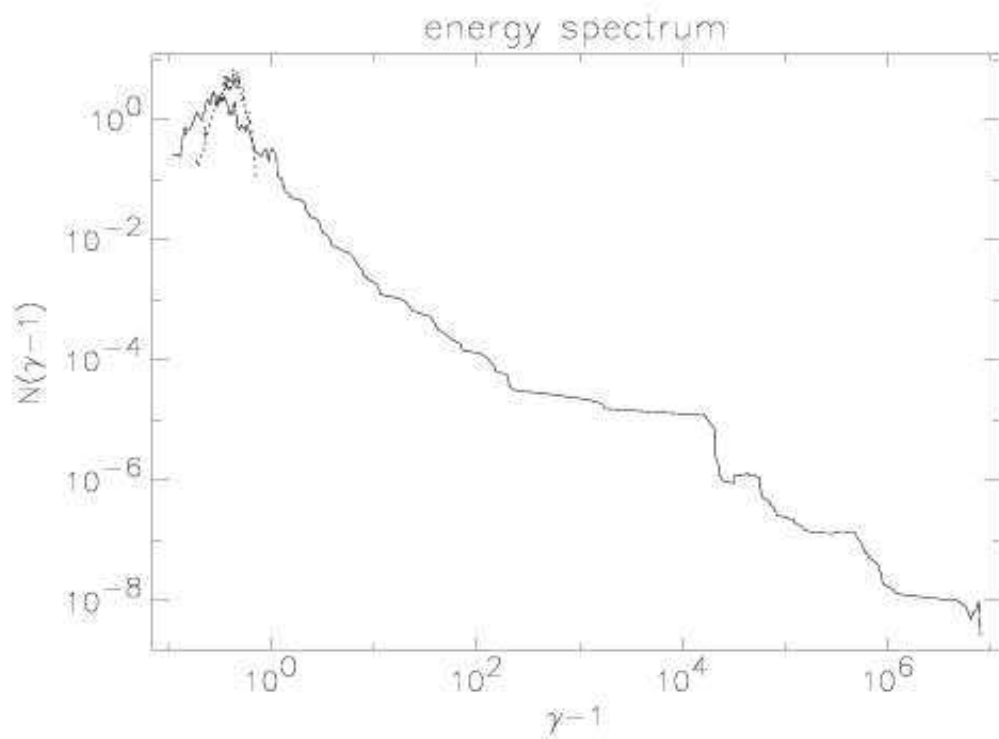


Fig. 24.

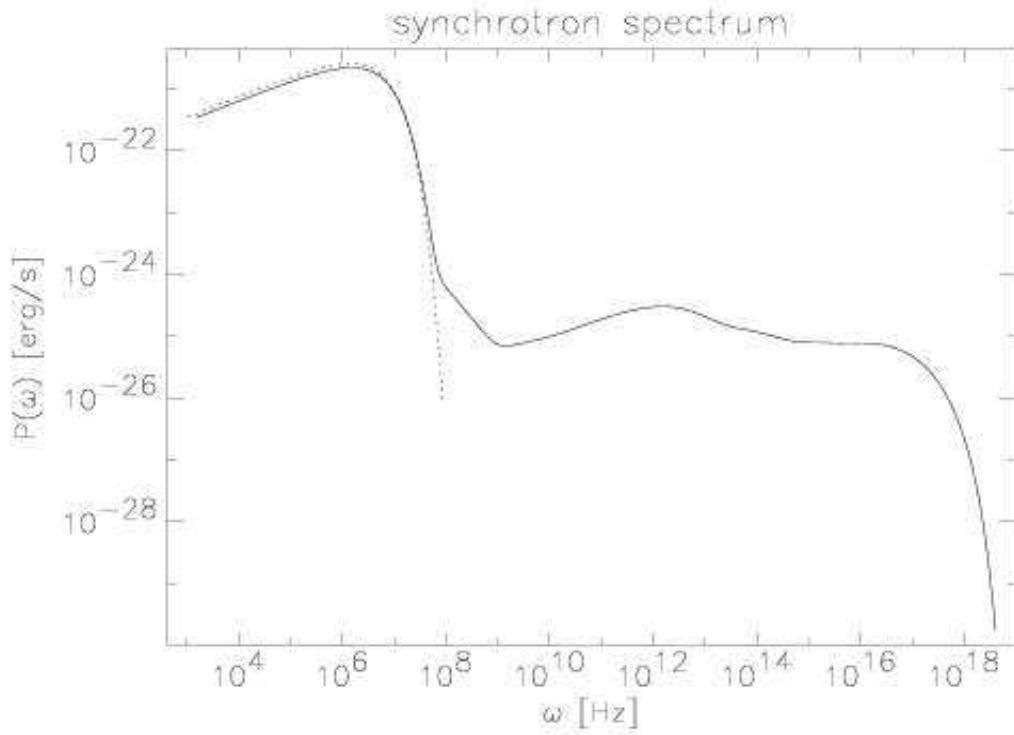


Fig. 25.

